Homogeneous and Nanogranular Prussian Blue to Enable Long-Term-Stable Electrochromic Devices

Xiaofang Fu, Kun Li, Chengli Zhang, Qiang Wang, Guanglong Xu, Alexander Alexandrovich Rogachev, Maxim Anatolievich Yarmolenko, Hongtao Cao, and Hongliang Zhang*

Read Online

ACCESS | Metrics & More | Article Recommendations | Supporting Information

ABSTRACT: The increasing demand for the state-of-the-art electrochromic devices has received great interest in synthesizing Prussian blue (PB) nanoparticles with a uniform diameter that exhibit excellent electrochromism, electrochemistry, and cyclability. Herein, we report the controllable synthesis of sub-100 nm PB nanoparticles via the coprecipitation method. The diameter of PB nanoparticles can be modulated by adjusting the reactant concentration, the selection of a chelator, and their purification. The self-assembled nanogranular thin films, homogeneously fabricated by using optimized PB nanoparticles with an average diameter of 50 nm as building blocks via the blade coating technique enable excellent performance with a large optical modulation of 80% and a high coloration efficiency of 417.79 cm^2 C^{-1}. It is also demonstrated by in situ and ex situ observations that the nanogranular PB thin films possess outstanding structural and electrochemical reversibility. Furthermore, such nanogranular PB thin films can enjoy the enhanced long-term cycling stability of the PB-WO$_3$ complementary electrochromic devices having a 91.4% optical contrast retention after 16,000 consecutive cycles. This work provides a newly and industrially compatible approach to producing a complementary electrochromic device with extraordinary durability for various practical applications.

KEYWORDS: prussian blue, nanoparticle, high coloration efficiency, electrochromic devices, long-term stability
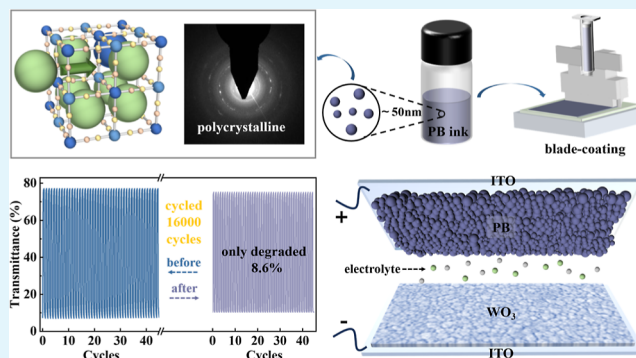
1. INTRODUCTION

Electrochromism refers to the phenomenon in which an applied electric field induces a stable and reversible change in the optical properties of the material.[1,2] Electrochromic devices have attracted widespread attention owing to their low energy consumption, low cost, and green in various applications such as smart windows,[3] information displays,[4] and antiglare rear-view mirrors.[5] Today, a wide variety of electrochromic materials including transition metal oxides (WO$_3$,[6] NiO$_x$[7] etc.), Prussian blue (PB) (iron(III) hexacyanoferrate(II), PB),[8] and conductive polymers (polyaniline (PANI))[9], have been extensively studied due to their impressive electrochromic properties. For example, a WO$_3$ quantum dot film has been reported to exhibit excellent electrochromic properties with high optical contrast (97.8% @ 633 nm), rapid switching speeds (4.5 s for coloring and 4 s for bleaching), and an exceptionally long cycle life (10,000 cycles with a 10% loss of optical contrast).[10] Among the numerous electrochromic materials, PB and tungsten oxide (WO$_3$) are both frequently used inorganic electrochromic materials due to their good optical memory effect, which enables the electrochromic device to maintain colored or bleached states without external energy consumption. The quest for a superior electrochromic material involves achieving high optical

modulation, excellent coloration efficiency, and long-term cycle stability, while supercapacitor materials aim for high capacity and enduring cycle stability. The exceptional capacity of PB as a supercapacitor material makes it an ideal match with high-capacity tungsten oxide, enabling the attainment of the superior performance required for electrochromism. Such device has shown enormous prospects in various highly desirable energy-efficient applications,[11] such as solving energy consumption problems through separate dynamic control of the transmission of visible and near-infrared light.[2] The crystal structure of PB exhibits an infinite three-dimensional network, which facilitates the rapid transport of ions because of its open ionic channels and spacious interstitial spaces. Its chemical compositions can be expressed as A$_x$Fe[Fe(CN)$_6$]·nH$_2$O (0 < x < 2), where A denotes an alkali metal cation in the gap such as Li$^+$, Na$^+$, K$^+$, etc.[12] During cation and electron insertion/

Scheme 1. Schematic Illustration of the Assembly of Long-Term-Stable ECDs Based on Homogeneous and Polycrystalline PB Nanoparticles
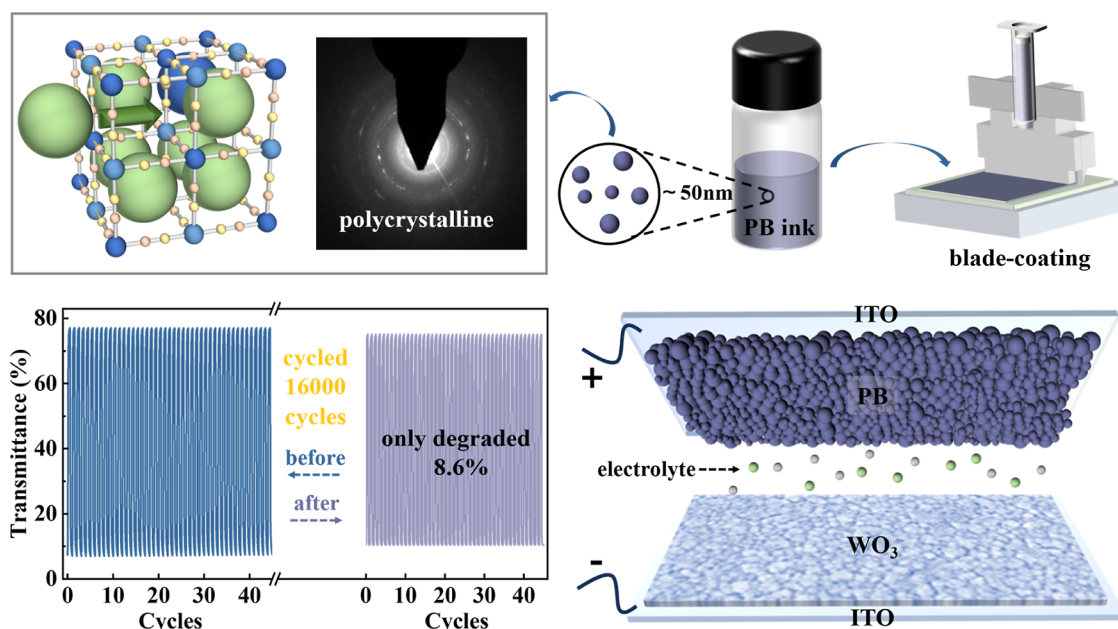
extraction, the Fe^{2+}/Fe^{3+} couple in the lattice skeleton can coherently change their valence to keep overall electroneutrality, accompanied by the bleaching/coloring process of PB.[13] Therefore, the electron transport efficiency and the ion diffusion distance determine the electrochromic performance of PB.[14] The composite of highly conductive materials has shown an enhancement of transfer of electrons and a synergistic effect for the PB films. For instance, it is demonstrated that a PB/TiO_2 film displayed outstanding optical modulation (85.4% @ 700 nm) and an improvement in the cyclic stability (83.8% optical contrast retention after 1000 cycles).[8] Another striking example is the CNT/PB nanocomposite films, which show a high coloration efficiency of 138.6 cm^2 C^{-1} and a fast response time within 3 s.[15] Nevertheless, the dopant-type PB composite films show limited electrochemical or electrochromic stability and durability.[14,16] In contrast, the nanostructured design of materials is another effective strategy to enhance the electrochromic performance of PB, which can not only shorten the ion transport distance but also increase the electrical conductivity by improving the homogeneity and compactness of the films.[17] It is reported that PB films with nanoparticles of sub-10 nm size exhibit a high coloration efficiency of 115.8 cm^2 C^{-1} and can be electrodeposited by using silicate sol−gel matrix as the solid-support.[18] However, such a technique for the PB films generally has a lack of uniformity in film thickness and composition, producing a substantial amount of unavoidable cracks and causing the unsatisfied cyclic stability with only 100 cycles.

Moreover, it is well-known that currently PB is conventionally deposited using electrodeposition and hydrothermal deposition methods, which require expensive equipment, additional electrical energy input, or harsh conditions of high temperature and pressure. These factors make it challenging to scale up production. To solve these issues, the preparation of films by blade coating with preformed PB nanoparticle ink is an attractive method that is not only compatible with the roll-to-roll process but also enables the preparation of nanostructured films and avoids the formation of cracks through synchronous heat treatment. Recently, the synthesis of small PB nanoparticles with

a diameter of tens of nanometers has been realized, which can meet the requirement for the production of PB-based electrochromic film.[19] The electrochromic device containing PB film based on nanoparticles of mean 10 nm size shows an excellent optical modulation of 62.5% with a high coloration efficiency of 157 cm^2 C^{-1} @ 545 nm, and a 94.2% optical contrast retention after 1000 cycles.[20] Currently, the key obstacle is to synthesize PB nanoparticles with a suitable size window that can determine their reversible electrochemical and electrochromic performance for electrochromic devices. Tuning the homogeneity of PB nanoparticles in size and composition is a key to overcoming the performance limits of PB as a counter electrode for electrochromic devices by various strategies adopted in reducing the reactant concentration, homogenizing precipitation, and preventing Ostwald ripening.[21] It should be noted that the concentration of reactants is not the smaller the better since an extremely low concentration leads to a decline in yield and production efficiency, which is unfavorable to the industrialization process. The principle of the homogeneous precipitation method is to select the optimized chelator to release the crystalline ions uniformly and slowly through chemical reaction, which can effectively prolong the characteristic nucleation time.[22] Reducing the reactant concentration and homogenizing precipitation involve the work before the reaction with sufficient time to prepare, preventing Ostwald ripening requires the separation of the nanoparticles from the mother liquor in a timely manner after the reaction, which can also be called a purification process.[23] Traditional purification processes take cycles of centrifugation, which is time-consuming and costly. A cross-flow filtration method has been developed to purify nanocrystals, but the success of this method depends on various parameters, such as the size of nanocrystals, flow rate, and pressure.[24] Therefore, it remains a challenge to develop a simple, convenient, and scalable filtration method.

Herein, we report a controllable synthesis of homogeneous and sub-100 nm PB nanoparticles with an average grain size of 50 nm via a sequential strategy that combines a coprecipitation synthetic process with a purification process. The nanogranular
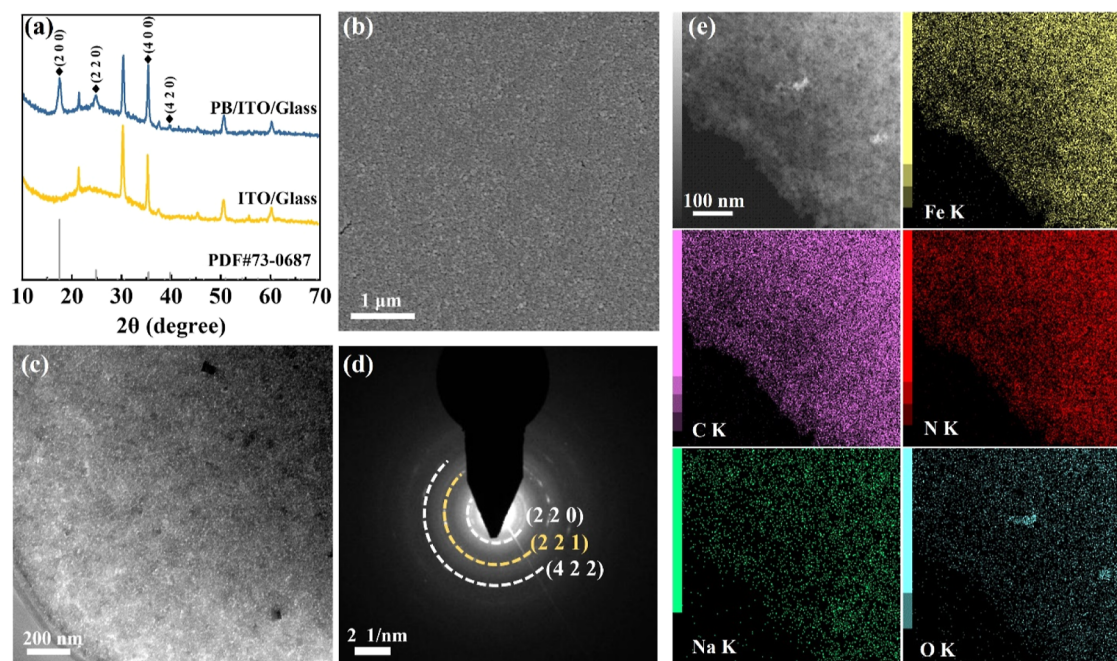
Figure 1. (a) XRD pattern and (b) top view SEM image of the PB/ITO/glass. (c) TEM image and (d) selected-area electron diffraction (SAED) patterns of the PB nanoparticles. (e) TEM image of the PB nanoparticles and the corresponding EDS elemental mapping images of Fe, C, N, Na, and O.

PB thin films fabricated by the blade coating method from precursor ink contained the PB nanoparticles, which enjoy an ultrahigh coloration efficiency (417.79 cm^2 C^{-1}) and an excellent long-term cycle stability (99.6% optical contrast retention after 1000 cycles). The complementary PB-WO$_3$ electrochromic devices fabricated by the nanogranular PB thin films manifest a high performance with an ultralong cyclic stability over 16,000 switching cycles, as depicted in Scheme 1.

2. EXPERIMENTAL SECTION

2.1. Materials. All chemicals were of analytical grade. Sodium ferrocyanide (Na$_4$[Fe(CN)$_6$]·10H$_2$O, AR) and citric acid (C$_6$H$_8$O$_7$, AR, ≥99.5%) were purchased from Macklin. Ferric nitrate (Fe(NO)$_3$·9H$_2$O, AR) was obtained from Aladdin. Both PB and WO$_3$ thin films were deposited on transparent conducting indium tin oxide (ITO)-coated glass substrates with a sheet resistance of 12 Ω/sq.

2.2. Preparation of the PB Nanoparticles. The preparation of PB nanoparticles was based on a typical coprecipitation method. Specifically, 1.0 mmol of citric acid (196 mg) was first added to 40 mL of 10 mM aqueous Fe(NO)$_3$·9H$_2$O solution (mixed solution I) under stirring at 60 °C. 40 mL portion of 10 mM aqueous Na$_4$[Fe(CN)$_6$]·10H$_2$O solution containing the same amount of citric acid (mixed solution II) was added dropwise to the mixed solution I under stirring at 60 °C, and then a dark blue dispersion was gradually formed. After stirring at 60 °C for 1 min, the solution was allowed to cool to room temperature. The solution was then transferred to a dialysis membrane (Spectra/POR6, MWCO = 3000) to be dialyzed against deionized water to remove excess impurity ions until the pH of the solution turned to neutral. Finally, the solution after dialyzing was freeze-dried under vacuum to obtain PB nanoparticles. The resulting PB nanoparticles had an average particle size of about 50 nm (Figure S1a), as determined by dynamic light scattering (DLS).

2.3. Preparation of the PB Thin Films. The powder of PB (1.0 g) was added into the aqueous solution of Na$_4$[Fe(CN)$_6$]·10H$_2$O (0.39 g, 15 mL of water) and stirred for 1 week at room temperature. The PB thin films were fabricated on the ITO-coated glass from the obtained precursor PB inks by the blade coating method using a flexible electronic printer (MP1100, Shanghai Mi fang Electronic Technology

Co., Ltd.). As a pretreatment of blade coating, the 35 × 45 mm^2 ITO substrate glass was cleaned using ethanol and deionized water. Finally, all of the PB thin films were dried at 60 °C under vacuum for 6 h and properly stored for further experiments.

2.4. Preparation of the WO$_3$ Thin Films and Assembly of PB-WO$_3$ Electrochromic Devices. The preparation of the WO$_3$ thin films and the assembly of PB-WO$_3$ electrochromic devices have been described in detail elsewhere.[25]

2.5. Measurements. The structure and morphology of the PB thin films were analyzed by X-ray diffraction (XRD, Bruker D8 Advance DaVinci using Cu Kα (λ = 0.154178 nm) radiation and a θ−2θ configuration), thermal field-emission scanning electron microscopy (TFESEM, S4800, Hitachi, Japan), and transmission electron microscopy (TEM, Tecnai F20, FEI, USA). DLS experiments were performed on a Zetasizer Nano ZS instrument (Malvern, UK). The chemical states and elements were analyzed by X-ray photoelectron spectroscopy (XPS, Axis Ultra DLD, Kratos, UK). Thermogravimetric measurement (TG) was conducted on a TGA thermogravimetric analyzer (TF209F1, NETZSCH, German) in nitrogen at a scan rate of 10 °C min^{-1} from room temperature to 800 °C. FTIR spectra were recorded by a micro-infrared spectrometer (Cary660, Agilent, USA). In situ Raman spectra were measured with a Renishaw inVia Reflex confocal microscopy Raman system (532 nm laser source) and an electrochemical workstation (CHI660D, Chen Hua Shanghai), where the Raman spectra were recorded one by one during a CV process (10 mV s^{-1}) in the potential range from −0.5 to +0.5 V and were captured every 10 s. In situ optical transmittance spectra were obtained via UV−vis-IR spectroscopy (PerkinElmer Lambda 950) and an electrochemical workstation (CHI660D, Chen Hua Shanghai). The electrochemical impedance spectra were measured on an electrochemical workstation (Zennium, IM6) in the frequency range from 100 mHz to 100 kHz. The electrochemical measurements of PB thin films were carried out by the electrochemical workstation with a three-electrode cell, where the PB thin films, platinum sheet, and KCl-saturated Ag/AgCl served as the working electrode, counter electrode, and reference electrode, respectively. One M LiClO$_4$−PC electrolyte with 0.01 M acetic acid played the role of an electrolyte. The electrochemical measurements of the complementary ECDs were carried out in the traditional two-electrode system.
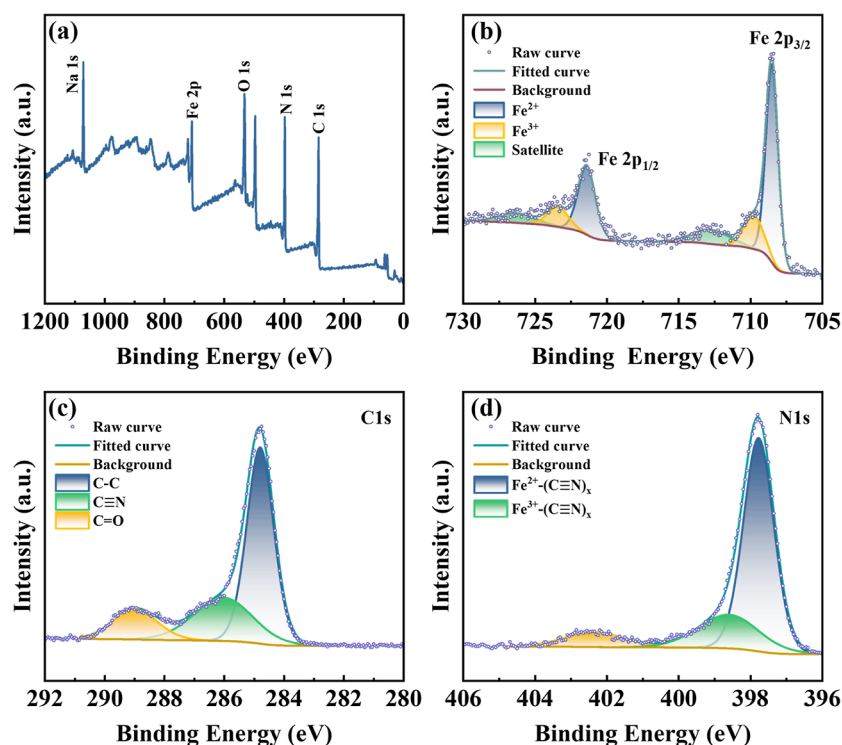
Figure 2. (a) Full XPS spectrum of the PB thin films. Fine XPS spectrum of (b) Fe 2p, (c) C 1s, and (d) N 1s in PB film.

3. RESULTS AND DISCUSSION

Figure 1a displays the XRD pattern of the PB thin films deposited on the ITO substrate, the peaks at diffraction angles of 17.5, 24.6, 35.2, and 39.5° can be, respectively, assigned to (200), (220), (400), and (420) of PB (JCPDS card no. 73-0687). In addition, these diffraction peaks are of low intensity and are broad, indicating a low crystallinity and small grain size. According to the Debye−Scherrer formula, the grain size is calculated to be about 12 nm (primary nanoparticles). The top-view SEM images at different magnifications are illustrated in Figures 1b and S2. The low magnification SEM image (Figure 1b) shows tightly packed nanoparticles with nanopores in the PB thin film. This homogeneous morphology structure formed by stacking nanoparticles provides an enlarged surface area, which facilitates electrolyte penetration and shortens the diffusion distance of conductive ions, leading to better electrochromic performance.[17] The nanoparticles with a homogeneous size distribution can be found in the high magnification SEM image (Figure S2). As shown in Figure S3, the height root-mean-square roughness (R_q) value of the PB thin films is determined to be 5.27 nm, which indicates that the surface of the film is uniform thanks to the close packing of nanoparticles as described in the SEM image. Based on the DLS data (Figure S1a), the PB particle size ranges from 10 to 100 nm and its average value is measured to be 50 nm. Such particles are believed to be formed from aggregates of the primary polycrystalline PB nanoparticles (12 nm). Both grain size and particle size belong to the sub-100 nm category. Based on the coating process, self-assembly of the sub-100 nm nanoparticles tends to fabricate homogeneous PB thin films with strong bonding forces to the substrate, resulting in high-performance electrochromism. The TEM image in Figure 1c also reveals that the PB is composed of nanoparticles. The selected area electron diffraction (SAED) pattern in Figure 1d indicates that the PB nanoparticles are polycrystalline, as evidenced by the presence of

both diffraction rings and spots. The diffraction rings correspond to the (200) and (220) planes of PB, consistent with the aforementioned XRD findings. The diffraction ring marked in yellow corresponds to the iron oxide phase, which most likely originated from a breakdown of PB due to its sensitivity to electron beam radiation. The EDS element diagram shown in Figure 1e demonstrates the uniform dispersion of Fe, N, C, Na, and O throughout the PB sample. The oxygen content can be mainly attributed to water molecules present in the PB lattice.

In general, PB is formed by alternating high-spin Fe^{3+} and low-spin Fe^{2+}, which are octahedrally coordinated by CN− and −CN units, respectively. Under electrochemical stimulation, PB can be readily reduced into Prussian white (reduction of high-spin Fe^{3+}) or sequentially oxidized into Berlin green (incomplete oxidation of low-spin Fe^{2+}) and Prussian yellow (complete oxidation of low-spin Fe^{2+}), delivering profound color variations between colorless, blue, green, and yellow.[13] For electrochromic devices, once the PB film reaches the Berlin green state, there is a loss of stability. Thus, in electrochromic applications, PB films are restricted to between PB and Prussian white.[26] To characterize the chemical composition of our PB films, the XPS test was studied. The full XPS spectrum of the PB thin films is depicted in Figure 2a. The full spectrum shows strong peaks at binding energies of 1071, 708, 532, 397, and 284 eV, corresponding to the Na 1s, Fe 2p, O 1s, N 1s, and C 1s signals, respectively. These signals are the principal constituent elements of PB, in accordance with the formula Na-$Fe^{III}[Fe^{II}(CN)_6] \cdot nH_2O$. The Fe 2p spectrum (Figure 2b) is composed of two regions representing the spin−orbital splitting components of Fe $2p_{3/2}$ and Fe $2p_{1/2}$. The binding energies located at 708.5 and 721.4 eV are attributed to Fe^{2+} $2p_{3/2}$ and Fe^{2+} $2p_{1/2}$, while the peaks at 709.8 and 723.4 eV correspond with Fe^{3+} $2p_{3/2}$ and Fe^{3+} $2p_{1/2}$, respectively. Meanwhile, the two remaining peaks at 712.8 and 726.4 eV could be explained as
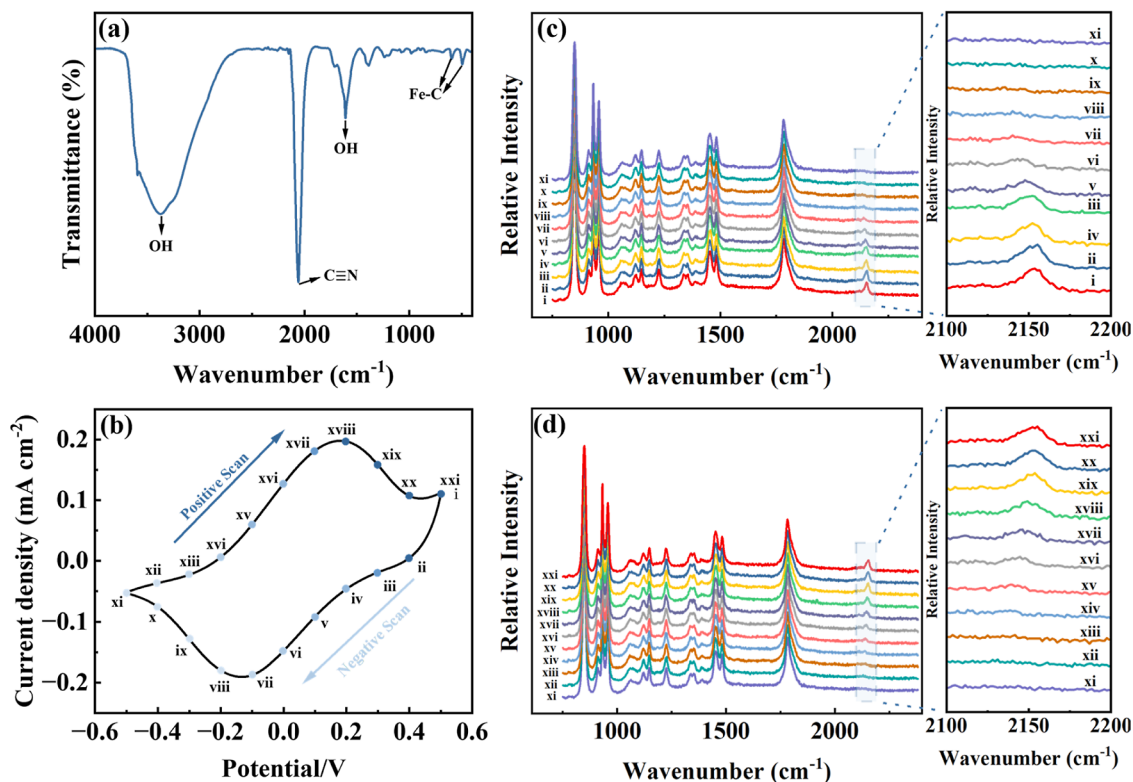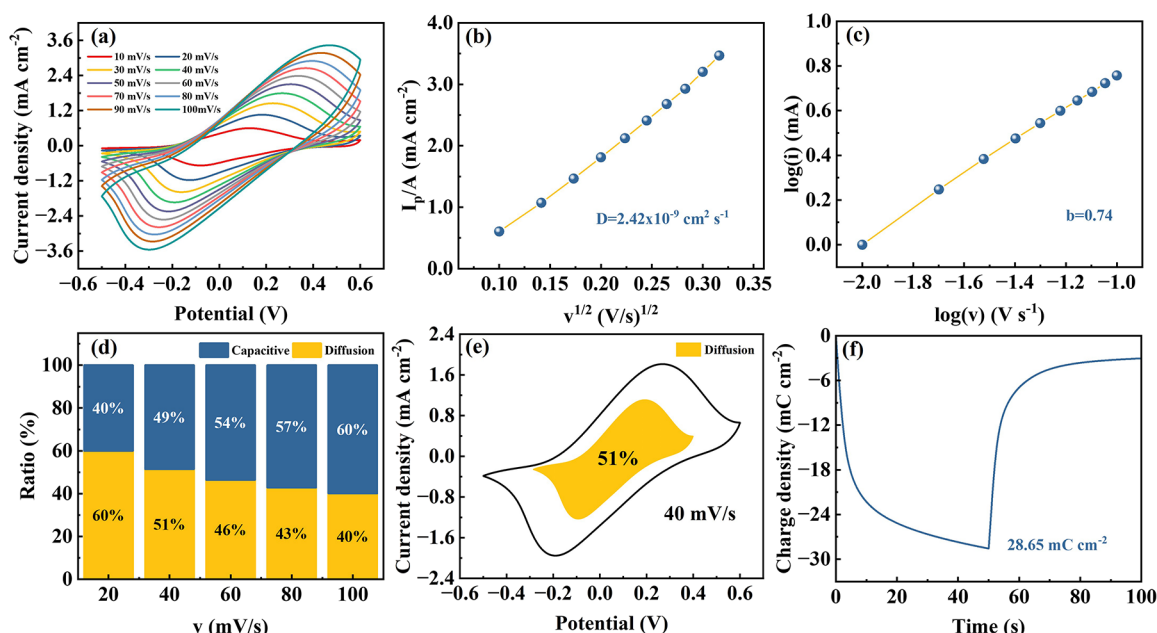
Figure 3. (a) FTIR spectra of the PB thin films. (b) Cyclic voltammograms (CVs) of the PB thin films between −0.5 V and +0.5 V at the scan rate of 10 mV s^{-1} in PC-LiClO$_4$ electrolyte with acetic acid. In situ Raman spectra of PB thin films during CV process in (c) negative-going and (d) positive-going sweeps.
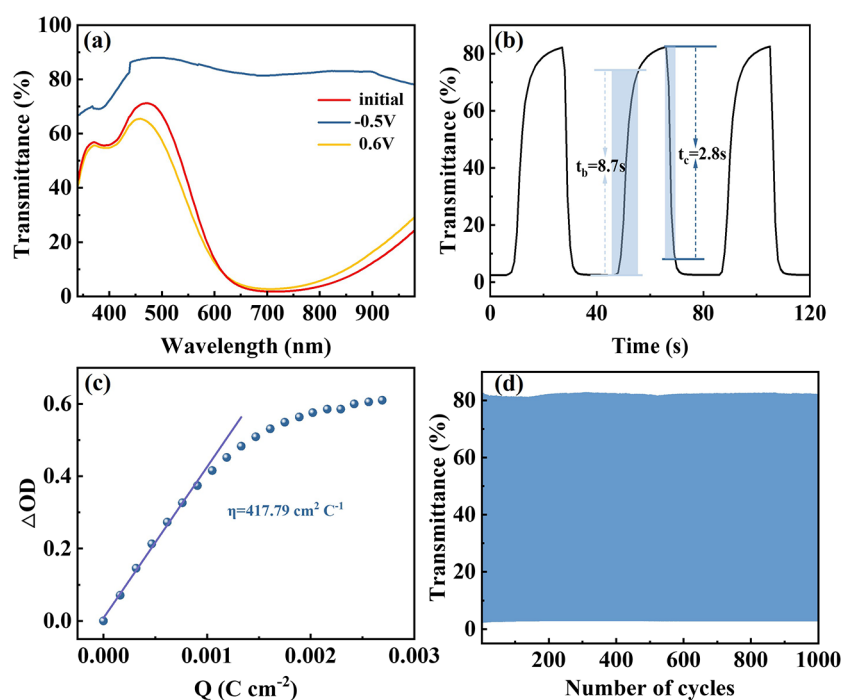
satellites associated with Fe^{2+}, which implied the partial reduction of high-spin Fe^{3+} to high-spin Fe^{2+}.[27] The C 1s spectrum can be deconvoluted to three peaks located at 284.8, 286.2, and 289.1 eV, assigned to the C−C, C≡N, and C=O bands, respectively (Figure 2c). The C−C, C≡N, and C=O peaks originate from intrinsic PB and the water molecules absorbed on the PB surface. The N 1s spectrum (Figure 2d) displays two peaks at 397.8 and 398.6 eV corresponding to the N in the cyanide bonded to Fe in different valence states, along with a weaker peak at 402.3 eV attributed to surface contaminants.[27,28] The XPS results elucidate the successful preparation of PB.

In order to investigate the ion transfer at the electrode−electrolyte interface during the electrochemical process, FTIR and in situ Raman tests were carried out. As shown in the FTIR spectra in Figure 3a, the prominent peak at 2059 cm^{-1} is attributed to the stretching vibration mode of C≡N.[29] Additionally, the peaks at 3380 and 1608 cm^{-1} represent the O−H stretching vibrations and bending modes, respectively.[30] These O−H bonds are associated with crystal water present in the framework. Actually, PB contains two types of water, namely, zeolite water adsorbed on the surface and coordination water in the framework. These two types of water decompose at temperatures above 100 and 200 °C, respectively. TG analysis (Figure S4) shows that the total weight loss ratio of PB is 6 and 21% at 100 and 200 °C, respectively. This implies that PB does contain a significant amount of coordination water. Imanishi et al.[31] have suggested that the greater the amount of water coordinated around Fe^{3+} ions in PB, the higher the capacity for lithium storage. This indicates that our PB thin films can have a high charge capacity. The two weak peaks at 594 and 496 cm^{-1} correspond to the in-plane and out-of-plane deformations of the
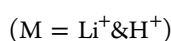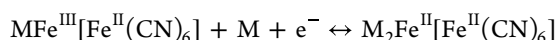
Fe−C bond, respectively.[32] The cyanide stretching vibration mode is very sensitive to its surrounding environment; thus, Raman spectroscopy can be used to identify the average valence states of transition metal ions coordinated with cyanide.[33] The Raman spectrum of the original PB thin film in PC-LiClO$_4$ electrolyte with acetic acid is plotted in Figure S5, and the peak at 2151 cm^{-1} refers to the 1A$_g$$v$(CN) stretching vibration and [Fe(II), Fe(III)] vibrational state. The peak presents a shoulder at 2117 cm^{-1}, which is characteristic of CN^{-}.[34] Figure 3c,d corresponds to the in situ Raman spectra (measured at intervals of 0.1 V) of the PB thin films during the CV (Figure 3b) process in the negative-going and the positive-going sweeps, respectively. As shown in Figure 3c, the representative peaks related to cyanide gradually shift to a lower wavenumber in the reduction process, while the intensity decreases significantly and finally disappears at viii. The C≡N banding to Fe^{2+} is usually present at lower wavenumbers than those coordinating to Fe^{3+}.[29] Therefore, we can infer that the gradual shift in the v(CN) frequency from high wavenumbers to lower wavenumbers could be an effect of changes in the average Fe valence states from +3 to +2. The change in the average Fe valence state is caused by the reduction of high-spin Fe due to the electron injection accompanying the intercalation of electrolyte ions into the PB thin film. On the contrary, the same peak (appearing at xiii) from Figure 3d gradually intensifies and moves toward a higher wavenumber during oxidation and eventually returns to the initial position. Overall, the shift of the peaks is caused by reversible intercalation/deintercalation of electrolyte ions into/from the PB thin film. Consequently, a potential electrochemical process of PB thin films circulating in PC-LiClO$_4$ electrolyte with acetic acid is outlined as the following reactions

Figure 4. (a) CVs of the PB thin films at scan rates of 10, 20, 30, 40, 50, 60, 70, 80, 90, and 100 mV s^{-1}. (b) Correlation between the peak current densities (i_p) and the square root of scan rate ($v^{1/2}$) and (c) the power law relationship between the peak currents and scan rates of the PB thin films in PC-LiClO$_4$ electrolyte with acetic acid. (d) Diffusion-controlled and surface capacitive behavior as percentages of the total capacitance at different scan rates. (e) CV curve at 40 mV s^{-1} illustrates the contribution of the surface capacitance to the total current (shadow area). (f) Charge density.

Figure 5. (a) Wavelength-dependent optical transmittance spectra. (b) Switching time and transmittance curves between the colored state and the bleached state at 700 nm (−0.5 V/+0.6 V, 40 s per cycle). (c) Plots of the time-dependent optical density variation as a function of charge density at 700 nm. (d) In situ time-dependent optical transmittance spectra at 700 nm (−0.5 V/+0.6 V, 40 s per cycle) for the PB thin films in PC-LiClO$_4$ electrolyte with acetic acid.

$$MFe^{III}[Fe^{II}(CN)_6] + M + e^- \leftrightarrow M_2Fe^{II}[Fe^{II}(CN)_6]$$

$$(M = Li^+ \& H^+)$$

(1)

Briefly, the cation exchange process of reactions in S6 can be completed in the first cycle of the PB thin films, and the

subsequent cycles can proceed reversibly in accordance with Reaction 1.

In order to understand the electrochemical reaction kinetics of the PB thin films in PC-LiClO$_4$ electrolyte with acetic acid, the CV curves (Figure 4a) are recorded at various scan rates between −0.5 and +0.6 V in the three-electrode system. Furthermore, the ion diffusion behaviors can be investigated by

Figure 6. (a) Nyquist plots of the PB thin films at constant potentials of +0.1, +0.2, +0.3, and +0.4 V; the insets show the Nyquist plots at +0.5 and +0.6 V and equivalent circuit model. (b) Nyquist plots of the PB thin films at constant potentials of 0, −0.1, −0.2, −0.3, −0.4, and −0.5 V; the inset shows the enlarged Nyquist plots in the high-frequency region.

the relationship between the peak current (i_p) and the corresponding scan rates (v). It is evident from Figure 4b that the peak current is proportional to the square root of the scan rate. On this basis, the diffusion coefficient is calculated to be 2.42×10^{-9} cm^2 s^{-1} according to the Randles−Sevcik equation.[35] In addition, the envelope area of the CV curve represents the contribution of the diffusion-controlled process and surface capacitance effect to total charge storage.[36] The faster the scan rate, the larger the enclosed area, indicating its pseudocapacitive behavior.[37] As the scan rate decreases, the redox peaks get closer, demonstrating that the influence of the diffusion-controlled process is enhanced at low scan rates.[38] Further, the proportion of diffusion-controlled process and surface capacitance dominant process can be determined by the following formula: $i_p = a \times v^b$, where a is an adjustable parameter and the b value is calculated from the slope of the linear plot of log i_p versus log v.[39] Commonly, the value of $b = 0.5$ represents the diffusion-controlled process, while $b = 1.0$ denotes the surface capacitance dominant process.[40] The value of b is calculated to be 0.74 (Figure 4c), confirming that the total capacity of the PB thin films is simultaneously controlled by diffusion-controlled and capacitor-like behaviors. The detailed charge storage contributions of the diffusion-controlled process and capacitive effect can be quantitatively calculated according to Dunn's method[41]

$$i_p = k_1 v + k_2 v^{1/2} \tag{2}$$

where $k_1 v$ and $k_2 v^{1/2}$ represent the effects of capacitance and diffusion processes, respectively. The calculation results (Figure 4d) indicate that the contribution related to diffusion increases with a decrease in the scan rate, as discussed earlier. When the scan rate is 40 mV/s, the proportion of the two parts is balanced (both are ∼50%) (Figure 4e). The charge density is obtained via the chronocoulometry method by supplying a square-wave voltage of −0.5 and +0.6 V with a pulse width of 45 s (Figure 4f). The maximum charge capacity for the PB thin films in PC-LiClO$_4$ electrolyte with acetic acid is calculated to be 28.65 mC cm^{-2}, higher than that reported in the previous literature.[42] Such high charge capacity can desirably match a high charge capacity of the electron beam evaporated WO$_3$ thin films (usually 35−40 mC cm^{-2}).
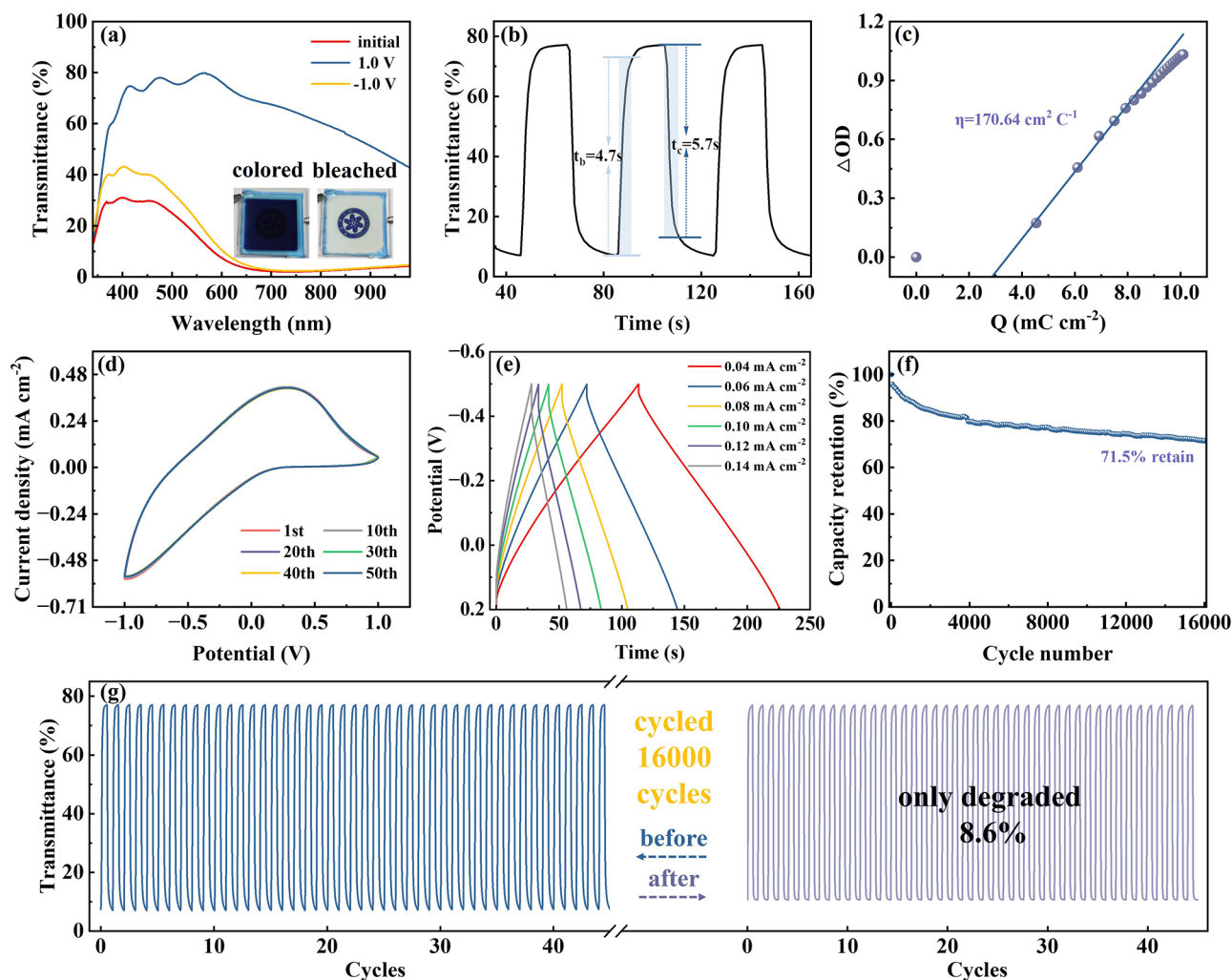
To evaluate the electrochromic performance of the PB thin films, the wavelength-dependent optical transmittance spectra in the PC-LiClO$_4$ electrolyte with acetic acid are shown in Figure 5a. An optical transmittance modulation (ΔT) of the nano-granular PB thin films between the bleached and the colored states is estimated to be 79.98% @ 700 nm, larger than the value

reported in the previous work.[43] The obtained high optical modulation is attributed to not only the synergistic effect of Li$^+$ and H$^+$ ions at the interface of the PB/electrolyte but also the huge specific surface area and more active sites of the PB thin films with tightly packed nanoparticles. Figure 5b shows the switching time and transmittance curves of the PB thin films at 700 nm. The colored/bleached response time, which is stipulated as the time required for the change in transmittance of the film to reach 90% between the colored and bleached states, is calculated to be 2.8 s/8.7 s for the PB thin films. Compared with the colored response time, the longer bleached time is inferred as a result of the significant difference in interface charge transfer resistance between the electrode and the electrolyte interface during the colored process and bleached process, which makes it more arduous for ions to intercalate into the film than the deintercalation of ions.[44] The coloration efficiency (η) is a key parameter to evaluate the electrochromic performance, which is defined as the change in optical density (ΔOD) caused by the charge stored per unit area (Q_s) of the PB thin film during the coloration process. It can be calculated by the following standard equation[45]

$$\eta = \frac{\Delta OD}{Q_s} = \frac{\log \frac{T_{bleached}}{T_{colored}}}{Q_s} \tag{3}$$

where $T_{bleached}$ and $T_{colored}$, respectively, represent the transmittance of the PB thin film in bleached and colored states. As shown in Figure 5c, the coloration efficiency of the PB thin film is estimated to be 417.79 cm^2 C^{-1}, much larger than that reported in the previous work.[46] The high coloration efficiency means a broad optical modulation within a small amount of charge variation.[47] Hence, the film accumulates less charge during the electrochromic cycle, coupled with the open framework and three-dimensional large pore structure of PB itself, which alleviates the structural stress generated during the ion intercalation/deintercalation process, which can theoretically arouse its long-term cyclic stability.[20] Surprisingly, excellent reversibility and cycling stability of the PB thin film are exhibited from its time-dependent optical transmittance curve, as shown in Figure 5d. It still retains original optical transmittance modulation (ΔT) after more than 1000 consecutive cycles, exhibiting remarkable long-term optical reversibility with a slight reduction from 79.3 to 79.0%.

The electrochemical impedance spectroscopy (EIS) was carried out to investigate the electrochemical behavior and interfacial properties of the PB thin films at different constant potentials with a signal amplitude of 10 mV in the frequency

Figure 7. (a) Wavelength-dependent optical transmittance spectra (the illustrations are digital photos of the different states), (b) switching time and transmittance curves between the colored state and the bleached state at 633 nm (−1 V/+1 V, 40 s per cycle), (c) plots of the time-dependent optical density variation as a function of charge density at 633 nm, (d) CVs at a scan rate of 100 mV s⁻¹, (e) GCD curves under diverse current densities, (f) cyclic performance at a current density of 0.08 mA cm², and (g) the optical contrast retention after 16,000 consecutive cycles for the PB-WO₃ complementary electrochromic devices.

range of 100 mHz to 100 kHz, as presented in Figure 6. The complete Nyquist plot consists of a semicircle in the high-frequency region and an inclined line in the low-frequency region, the former being related to the charge transfer process at the interface, and the latter being correlated with the ion diffusion process.[48] One can readily be seen that quite a few curves in Figure 6b only show a semicircular region with no incline lines, which is due to the fact that the interfacial charge transfer resistance at the corresponding voltage is too large to capture enough low-frequency information in the measured frequency range. The equivalent circuit diagram obtained from the Nyquist curve simulation is shown in Figure 6a, and the corresponding electrical parameters are given in Table S1. Among them, Warburg impedance (W) reflects the diffusion kinetics of electrolyte ions in PB thin films.[49] The interfacial charge transfer resistance (R_{ct})[50] at the electrode−electrolyte interface corresponds to the diameter of the semicircle in the high-frequency region of the Nyquist plot, and the electrolyte resistance (R_s)[51] can be obtained from the intersection of the Nyquist plot and the real axis. Specifically, there is no significant change in the value of R_s under different bias voltages, while the R_{ct} values under negative bias voltages are much larger than

those under positive bias voltages. According to the in situ Raman analysis aforementioned, a large amount of electrolyte ions is intercalated in the PB three-dimensional framework under negative bias voltages, resulting in the transformation of PB into Prussian white. Based on the UV visible spectra, the optical band gap of colored state (PB) and the bleached state (Prussian white) of the electrochromic films is, respectively, calculated to be 2.05 and 3.38 eV (Figure S7), similar to those in the previous report.[52] An increase in the band gap is believed to give rise to fewer free electrons and reduced electrical conductivity.[53] The lower conductivity of Prussian white leads to a slow migration rate of electrolyte ions at the electrode−electrolyte interface, and an increase in the interfacial charge transfer resistance.[54] One reason why the coloring response time of PB thin films is much shorter than the bleached response time is that high conductivity leads to faster reduction/oxidation behavior and a shorter response time. The R_{ct} at the voltage of −0.1 V is located in the middle value, indicating that the thin film is in the middle state between PB and Prussian white. When the voltage exceeds +0.4 V, there is a significant increase in the interfacial charge transfer resistance. It is speculated that part of

Table 1. Comparison of Electrochromic Performance between This Work and Other Reported Works

electrode materials	ΔT (%) @ wavelength (nm)	coloration efficiency (cm² C⁻¹)	switching time (s)		cyclic stability (cycles)	optical contrast retention (%)	capacitance retention (%)	ref
			bleaching	coloring				
WO₃·H₂O/PW	61.7 @ 650	139.4	1.84	1.95	2500	82.5		57
WO₃/PANI	54.3 @ 633		1.4	1.1	2500	74.6		58
WO₃/Zn	77 @ 632.8		5.7	10.3	200	57.0		59
PW-MnO₂/WO₃	35 @ 510	77.6			10,000	62.0		60
AP-WO₃/NiO	60.7 @ 633		6.4	7.2	1000		60.2	61
PB/Zn	84.9 @ 633	76.8	4.6	4.1	7000	92.7	60.7	62
PB/PFSA	78.5 @ 633	75.75	13	51	300	76.9		63
PB/Li₄Ti₅O₁₂	55.3 @ 529	170.1	40	49.2	1000	95.8		64
WO₃/NiO	46 @ 633		3.1	4.6	2500	93		65
PB-NiO/WO₃	67.6 @ 630	110	2.8	7.9	4000	84	91	66
PB-NiO/Zn	73.2 @ 632.8	54.9	2.6	1.4	1000	92		67
Zn−CuZn/PB			3	7	1000			68
PB/Zn	83 @ 632.8		8.4	3				69
PB/Zn mesh	67.2 @ 632.8	131.5	2.5	3.6				70
PB/WO₃	70 @ 633	170.6	5.7	4.7	16,000	91.4	71.5	this work

Fe²⁺ in the low-spin state may be oxidized to Fe³⁺ at this time, resulting in a decrease in the conductivity of the thin film.[52]

In order to evaluate the rationality of using the PB thin films as the counter electrode for electrochromic devices, the PB thin film is incorporated in an electrochromic device with an electron beam evaporated WO₃ thin film. Figure 7a depicts the wavelength-dependent optical transmittance spectra of the device at diffident states. The PB-WO₃ device presents a noticeable electrochromism with an optical modulation of 70.07%, which is quite satisfying in electrochromic applications. At the same time, well-performing EC devices should be able to maintain their optical constants in the open-circuit state for a sufficiently long time without constantly consuming external energy. Figure S8 shows the change in the transmittance with the increase in open-circuit time for the PB-WO₃ complementary electrochromic device for a period of 16 h. For the bleached state, the optical transmittance variation is obvious by 8.68% within 1 h and only 2.54% in the following 15 h. The most significant change in colored state is in the first 2 h at 7%, while the final change after 16 h is 11.24%. The response times for coloring and bleaching are extremely short with 5.7 and 4.7 s (Figure 7b), faster than those of the reported PB-WO₃ devices.[55] Figure 7c presents the plots of the time-dependent optical density variation as a function of charge density at 633 nm. The value of coloration efficiency can be accordingly extracted from the slope of the linear region of the line, obtaining 170.64 cm² C⁻¹, larger than those reported in the previous works.[43,56] From Figure 7d, it can be observed that there is no significant change in the shape and envelope area of the CV plot after 100 cycles, indicating that the electroactivity of the devices has not decreased and the PB-WO₃ device has excellent electrochemical stability. Figure 7e depicts the galvanostatic charge/discharge (GCD) curves of the electrochromic device recorded at diverse current densities from 0.04 to 0.14 mA cm⁻², with the relatively symmetrical triangles indicating a reversible redox reaction. The areal capacitance (C_A, mF cm⁻²) can be calculated from the GCD profiles by the following equation

$$C_A = \frac{I\Delta t}{\Delta VS} \tag{4}$$

where I is the discharge current (mA), Δt is the discharge time (s), ΔV is the potential window (V), and S is the electrode area (cm²). Based on the discharge profiles, the areal capacitance is estimated to be, respectively, 6.45, 6.20, 5.99, 5.96, 5.78, and 5.60 mF cm⁻² at 0.04, 0.06, 0.08, 0.10, 0.12, and 0.14 mA cm⁻² (Figure S9), close to those of previously reported PB-WO₃ complementary electrochromic devices.[57] Furthermore, the PB-WO₃ complementary electrochromic device, possesses excellent long-cycle stability with 71.5% capacitance retention (Figure 7f) and 91.4% optical contrast retention (Figure 7g) after 16,000 consecutive cycles (27 days) by means of constant charge/discharge measurement at a current density of 0.08 mA cm⁻². The electrochemical switching mechanism of WO₃ and PB in the electrochromic process is schematically illustrated in Figure S10. Overall, the electrochromic and pseudocapacitive behavior of WO₃ and PB is both due to chemical reversible redox reactions of W(VI)/W(V) or Fe(II)/Fe(III), accompanied by the insertion/disinsertion of cation M, as shown in eqs 1 and 5[25]

$$WO_3 + xe^- + xM \leftrightarrow M_xWO_3 \tag{5}$$
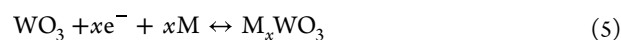
The comparison between the proposed ECD and those in the previous work is summarized in Table 1.

4. CONCLUSIONS

In summary, homogeneous and sub-100 nm PB nanoparticles with an average diameter of 50 nm can be synthesized using a sequential strategy combined by a coprecipitation process and a purification process. Our findings demonstrate that dialysis filtration is an efficient method to purify PB nanoparticles. Relying on the PB nanoparticle merits that can offer a highly compact and uniform PB host, a high specific surface, and more active sites for Li⁺ and H⁺ guest ions, the nanogranular PB thin films can achieve a large optical modulation of 80% and an ultrahigh coloration efficiency of 417.79 cm² C⁻¹. Quantitative electrochemical and electrochromic characteristics are further analyzed by using in situ spectroelectrochemistry in combination with ex situ analyses. Impressively, the highly reversible PB-WO₃ electrochromic devices can enjoy a high performance with a high coloration efficiency of 170.6 cm² C⁻¹ and an improved long cycling stability (at least 16,000 cycles with only 8.6% decay). The academic development in this work provides a

theoretical and experimental basis for the roll-to-roll process of electrochromic devices using PB precursors in the future.

■ ASSOCIATED CONTENT

Ⓢ Supporting Information

The Supporting Information is available free of charge at https://pubs.acs.org/doi/10.1021/acsami.3c17551.

> CVs of the PB thin films based on different-sized nanoparticles, SEM image of the PB thin films, TG curve of the PB nanoparticles, Raman spectra of the PB thin films in PC-LiClO$_4$ electrolyte with acetic acid, absorbance of the PB thin films, band gap of PB and PW thin films, bistability of PB-WO$_3$ ECDs, areal capacitances of PB-WO$_3$ ECDs, electrochemical switching mechanism of the WO$_3$ and PB, and electrical parameters obtained from EIS measurement of the PB thin film (PDF)

■ AUTHOR INFORMATION

Corresponding Author

Hongliang Zhang — *Laboratory of Advanced Nano Materials and Devices, Ningbo Institute of Materials Technology and Engineering, Chinese Academy of Sciences, Ningbo 315201, PR China; Center of Materials Science and Optoelectronics Engineering, University of Chinese Academy of Sciences, Beijing 100049, PR China;* ⓞ orcid.org/0000-0002-9295-8683; Phone: +86 574 86688153; Email: zhanghl@nimte.ac.cn; Fax: +86 574 86688163

Authors

Xiaofang Fu — *Laboratory of Advanced Nano Materials and Devices, Ningbo Institute of Materials Technology and Engineering, Chinese Academy of Sciences, Ningbo 315201, PR China; Center of Materials Science and Optoelectronics Engineering, University of Chinese Academy of Sciences, Beijing 100049, PR China*

Kun Li — *Vallight Optics Technology Ningbo Co., Ltd, Ningbo 315400, PR China*

Chengli Zhang — *Ningbo Wakan Electronic Science Technology Co., Ltd, Ningbo 315475, PR China*

Qiang Wang — *Ningbo Wakan Electronic Science Technology Co., Ltd, Ningbo 315475, PR China*

Guanglong Xu — *Ningbo Wakan Electronic Science Technology Co., Ltd, Ningbo 315475, PR China*

Alexander Alexandrovich Rogachev — *Optical Anisotropic Films Laboratory, Institute of Chemistry of New Materials of the National Academy of Sciences of Belarus, Minsk 220141, Belarus;* ⓞ orcid.org/0000-0003-4993-0519

Maxim Anatolievich Yarmolenko — *Francisk Skorina Gomel State University, Gomel 246019, Belarus;* ⓞ orcid.org/0000-0002-1283-8762

Hongtao Cao — *Laboratory of Advanced Nano Materials and Devices, Ningbo Institute of Materials Technology and Engineering, Chinese Academy of Sciences, Ningbo 315201, PR China; Center of Materials Science and Optoelectronics Engineering, University of Chinese Academy of Sciences, Beijing 100049, PR China*

Complete contact information is available at:
https://pubs.acs.org/10.1021/acsami.3c17551

Notes

The authors declare no competing financial interest.

■ ACKNOWLEDGMENTS

■ REFERENCES

(1) Liu, G. S.; Liu, C.; Chen, H. J.; Cao, W.; Qiu, J. S.; Shieh, H. P. D.; Yang, B. R. Electrically robust silver nanowire patterns transferrable onto various substrates. *Nanoscale* **2016**, *8* (10), 5507−5515.

(2) Wang, Z.; Zhang, Q.; Cong, S.; Chen, Z.; Zhao, J.; Yang, M.; Zheng, Z.; Zeng, S.; Yang, X.; Geng, F.; et al. Using Intrinsic Intracrystalline Tunnels for Near-Infrared and Visible-Light Selective Electrochromic Modulation. *Adv. Opt. Mater.* **2017**, *5* (11), 1700194.

(3) Li, H. Z.; Zhang, W.; Elezzabi, A. Y. Transparent Zinc-Mesh Electrodes for Solar-Charging Electrochromic Windows. *Adv. Mater.* **2020**, *32* (43), 10.

(4) Gu, C.; Jia, A. B.; Zhang, Y. M.; Zhang, S. X. A. Emerging Electrochromic Materials and Devices for Future Displays. *Chem. Rev.* **2022**, *122* (18), 14679−14721.

(5) Araki, S.; Nakamura, K.; Kobayashi, K.; Tsuboi, A.; Kobayashi, N. Electrochemical Optical-Modulation Device with Reversible Transformation Between Transparent, Mirror, and Black. *Adv. Mater.* **2012**, *24* (23), OP122−OP126.

(6) Li, Z. X.; Liu, Z. F.; Zhao, L.; Chen, Y.; Li, J. W.; Yan, W. G. Efficient electrochromic efficiency and stability of amorphous/crystalline tungsten oxide film. *J. Alloys Compd.* **2023**, *930*, 167405.

(7) Zhao, Y. M.; Zhang, X.; Chen, X.; Li, W. J.; Wang, L. B.; Li, Z. T.; Zhao, J. P.; Endres, F.; Li, Y. Preparation of Sn-NiO films and all-solid-state devices with enhanced electrochromic properties by magnetron sputtering method. *Electrochim. Acta* **2021**, *367*, 137457.

(8) Xu, H. B.; Gong, L. T.; Zhou, S. Y.; Cao, K. L.; Wang, S.; Zhao, J. P.; Li, Y. Enhancing the electrochromic stability of Prussian blue based on TiO$_2$ nanorod arrays. *New J. Chem.* **2020**, *44* (6), 2236−2240.

(9) Zhou, K. L.; Wang, H.; Jiu, J. T.; Liu, J. B.; Yan, H.; Suganuma, K. Polyaniline films with modified nanostructure for bifunctional flexible multicolor electrochromic and supercapacitor applications. *Chem. Eng. J.* **2018**, *345*, 290−299.

(10) Yao, Y. J.; Zhao, Q.; Wei, W.; Chen, Z.; Zhu, Y.; Zhang, P.; Zhang, Z. T.; Gao, Y. F. WO$_3$ quantum-dots electrochromism. *Nano Energy* **2020**, *68*, 104350.

(11) Besnardiere, J.; Ma, B. H.; Torres-Pardo, A.; Wallez, G.; Kabbour, H.; Gonzalez-Calbet, J. M.; Von Bardeleben, H. J.; Fleury, B.; Buissette, V.; Sanchez, C.; et al. Structure and electrochromism of two-dimensional octahedral molecular sieve h '-WO$_3$. *Nat. Commun.* **2019**, *10*, 327.

(12) Qian, J. F.; Wu, C.; Cao, Y. L.; Ma, Z. F.; Huang, Y. H.; Ai, X. P.; Yang, H. X. Prussian Blue Cathode Materials for Sodium-Ion Batteries and Other Ion Batteries. *Adv. Energy Mater.* **2018**, *8* (17), 24.

(13) Qiu, M.; Zhou, F.; Sun, P.; Chen, X.; Zhao, C.; Mai, W. Unveiling the electrochromic mechanism of Prussian Blue by electronic transition analysis. *Nano Energy* **2020**, *78*, 105148.

(14) Xu, M.; Wang, S.; Zhou, S. Y.; Ding, Z. M.; Xu, H. B.; Zhao, J. P.; Li, Y. Fast-Switching Speed and Ultralong Lifespan Au/Prussian Blue Electrochromic Film for Iris Devices Applications. *Adv. Mater. Interfaces* **2023**, *10* (7), 9.

(15) Nossol, E.; Zarbin, A. J. G. Electrochromic properties of carbon nanotubes/Prussian blue nanocomposite films. *Sol. Energy Mater. Sol. Cells* **2013**, *109*, 40−46.

(16) Zhang, Q.; Li, X.; Qin, M. M.; Guan, F. L.; Gong, Y.; Wang, R.; Xu, J.; Chen, G. M. Preparation of a PB@SiO$_2$ Photonic Crystal Composite with Enhanced Electrochromic Performance. *ACS Appl. Electron. Mater.* **2021**, *3* (10), 4441−4447.

(17) Isfahani, V. B.; Memarian, N.; Dizaji, H. R.; Arab, A.; Silva, M. M. The physical and electrochromic properties of Prussian Blue thin films electrodeposited on ITO electrodes. *Electrochim. Acta* **2019**, *304*, 282−291.

(18) Manivannan, S.; Kim, H.; Viswanathan, P.; Yim, T.; Kim, K. Spectroelectrochemical Studies on Silicate Sol-Gel Matrix-Supported

Sub-10 nm Prussian Blue Nanostructures-based Electrochromic Device. *Electroanalysis* **2020**, *32* (7), 1571−1581.

(19) Lee, K. M.; Tanaka, H.; Takahashi, A.; Kim, K. H.; Kawamura, M.; Abe, Y.; Kawamoto, T. Accelerated coloration of electrochromic device with the counter electrode of nanoparticulate Prussian blue-type complexes. *Electrochim. Acta* **2015**, *163*, 288−295.

(20) Fan, M.-S.; Kao, S.-Y.; Chang, T.-H.; Vittal, R.; Ho, K.-C. A high contrast solid-state electrochromic device based on nano-structural Prussian blue and poly(butyl viologen) thin films. *Sol. Energy Mater. Sol. Cells* **2016**, *145*, 35−41.

(21) Saad, W. S.; Prud'homme, R. K. Principles of nanoparticle formation by flash nanoprecipitation. *Nano Today* **2016**, *11* (2), 212−227.

(22) Shokouhimehr, M.; Soehnlen, E. S.; Hao, J. H.; Griswold, M.; Flask, C.; Fan, X. D.; Basilion, J. P.; Basu, S.; Huang, S. D. Dual purpose Prussian blue nanoparticles for cellular imaging and drug delivery: a new generation of T-1-weighted MRI contrast and small molecule delivery agents. *J. Mater. Chem.* **2010**, *20* (25), 5251−5259.

(23) Marqusee, J. A.; Ross, J. Theory of Ostwald ripening: Competitive growth and its dependence on volume fraction. *J. Chem. Phys.* **1984**, *80* (1), 536−543.

(24) Niu, G. D.; Zhang, L.; Ruditskiy, A.; Wang, L. D.; Xia, Y. N. A Droplet-Reactor System Capable of Automation for the Continuous and Scalable Production of Noble-Metal Nanocrystals. *Nano Lett.* **2018**, *18* (6), 3879−3884.

(25) Wang, K.; Zhang, H. L.; Chen, G. X.; Tian, T.; Tao, K.; Liang, L. Y.; Gao, J. H.; Cao, H. T. Long-term-stable WO_3-PB complementary electrochromic devices. *J. Alloys Compd.* **2021**, *861*, 158534.

(26) DeLongchamp, D. M.; Hammond, P. T. High-contrast electrochromism and controllable dissolution of assembled Prussian blue/polymer nanocomposites. *Adv. Funct. Mater.* **2004**, *14* (3), 224−232.

(27) Forment-Aliaga, A.; Weitz, R. T.; Sagar, A. S.; Lee, E. J. H.; Konuma, M.; Burghard, M.; Kern, K. Strong p-Type Doping of Individual Carbon Nanotubes by Prussian Blue Functionalization. *Small* **2008**, *4* (10), 1671−1675.

(28) Cano, A.; Rodriguez-Hernandez, J.; Reguera, L.; Rodriguez-Castellon, E.; Reguera, E. On the Scope of XPS as Sensor in Coordination Chemistry of Transition Metal Hexacyanometallates. *Eur. J. Inorg. Chem.* **2019**, *2019* (13), 1724−1732.

(29) Ojwang, D. O.; Haggstrom, L.; Ericsson, T.; Angstrom, J.; Brant, W. R. Influence of sodium content on the thermal behavior of low vacancy Prussian white cathode material. *Dalton Trans.* **2020**, *49* (11), 3570−3579.

(30) Avila, M.; Reguera, L.; Rodríguez-Hernández, J.; Balmaseda, J.; Reguera, E. Porous framework of $T_2[Fe(CN)_6] \cdot xH_2O$ with T = Co, Ni, Cu, Zn, and H2 storage. *J. Solid State Chem.* **2008**, *181* (11), 2899−2907.

(31) Imanishi, N.; Morikawa, T.; Kondo, J.; Takeda, Y.; Yamamoto, O.; Kinugasa, N.; Yamagishi, T. Lithium intercalation behavior into iron cyanide complex as positive electrode of lithium secondary battery. *J. Power Sources* **1999**, *79* (2), 215−219.

(32) Shen, L.; Wang, Z. X.; Chen, L. Q. Prussian Blues as a Cathode Material for Lithium Ion Batteries. *Chem.—Eur. J.* **2014**, *20* (39), 12559−12562.

(33) You, Y.; Yu, X. Q.; Yin, Y. X.; Nam, K. W.; Guo, Y. G. Sodium iron hexacyanoferrate with high Na content as a Na-rich cathode material for Na-ion batteries. *Nano Res.* **2015**, *8* (1), 117−128.

(34) Moretti, G.; Gervais, C. Raman spectroscopy of the photosensitive pigment Prussian blue. *J. Raman Spectrosc.* **2018**, *49* (7), 1198−1204.

(35) Yu, H.; Guo, J. J.; Wang, C.; Zhang, J. Y.; Liu, J.; Zhong, X. L.; Dong, G. B.; Diao, X. G. High performance in electrochromic amorphous WO_x film with long-term stability and tunable switching times via Al/Li-ions intercalation/deintercalation. *Electrochim. Acta* **2019**, *318*, 644−650.

(36) Liu, L.; Zhang, Q. Q.; Du, K.; He, Z. B.; Wang, T.; Yi, Y.; Wang, M. Y.; Zhong, X. L.; Dong, G. B.; Diao, X. G. An intelligent and portable

power storage device able to visualize the energy status. *J. Mater. Chem. A* **2019**, *7* (40), 23028−23037.

(37) Zhou, D.; Che, B. Y.; Kong, J. H.; Lu, X. H. A nanocrystalline tungsten oxide electrochromic coating with excellent cycling stability prepared via a complexation-assisted sol-gel method. *J. Mater. Chem. C* **2016**, *4* (34), 8041−8051.

(38) Liu, L.; Diao, X. G.; He, Z. B.; Yi, Y.; Wang, T.; Wang, M. Y.; Huang, J. L.; He, X. S.; Zhong, X. L.; Du, K. High-performance all-inorganic portable electrochromic Li-ion hybrid supercapacitors toward safe and smart energy storage. *Energy Storage Mater.* **2020**, *33*, 258−267.

(39) Yang, P. H.; Sun, P.; Du, L. H.; Liang, Z. M.; Xie, W. G.; Cai, X.; Huang, L. H.; Tan, S. Z.; Mai, W. J. Quantitative Analysis of Charge Storage Process of Tungsten Oxide that Combines Pseudocapacitive and Electrochromic Properties. *J. Phys. Chem. C* **2015**, *119* (29), 16483−16489.

(40) Brezesinski, T.; Wang, J.; Polleux, J.; Dunn, B.; Tolbert, S. H. Templated Nanocrystal-Based Porous TiO_2 Films for Next-Generation Electrochemical Capacitors. *J. Am. Chem. Soc.* **2009**, *131* (5), 1802−1809.

(41) Kim, J. W.; Augustyn, V.; Dunn, B. The Effect of Crystallinity on the Rapid Pseudocapacitive Response of Nb_2O_5. *Adv. Energy Mater.* **2012**, *2* (1), 141−148.

(42) Fu, Z. Y.; Wei, Y. X.; Liu, W. M.; Li, J. Y.; Li, J. M.; Ma, Y. B.; Zhang, X. F.; Yan, Y. Investigation of electrochromic device based on multi-step electrodeposited PB films. *Ionics* **2021**, *27* (10), 4419−4427.

(43) Ding, Y. L.; Wang, M. Y.; Mei, Z. Y.; Diao, X. A. Flexible Inorganic All-Solid-State Electrochromic Devices toward Visual Energy Storage and Two-Dimensional Color Tunability. *ACS Appl. Mater. Interfaces* **2023**, *15* (12), 15646−15656.

(44) Mohammadian, M.; Rashid-Nadimi, S.; Peimanifard, Z. Fluorine-doped tin oxide/hematite/Ni(OH)$_2$/Prussian white photo-electrode for use in a visible-light-assisted pseudocapacitor. *J. Power Sources* **2019**, *426*, 40−46.

(45) Xie, S. J.; Bi, Z. J.; Chen, Y. B.; He, X. L.; Guo, X. X.; Gao, X. D.; Li, X. M. Electrodeposited Mo-doped WO_3 film with large optical modulation and high areal capacitance toward electrochromic energy-storage applications. *Appl. Surf. Sci.* **2018**, *459*, 774−781.

(46) Zhang, W.; Li, H. Z.; Elezzabi, A. Y. A Dual-Mode Electrochromic Platform Integrating Zinc Anode-Based and Rocking-Chair Electrochromic Devices. *Adv. Funct. Mater.* **2023**, *33* (24), 12.

(47) Yang, Y. X.; Peng, Y.; Jian, Z. L.; Qi, Y. Y.; Xiong, Y. L.; Chen, W. Novel High-Performance and Low-Cost Electrochromic Prussian White Film. *ACS Appl. Mater. Interfaces* **2022**, *14* (6), 8157−8162.

(48) Narayanan, R.; Dewan, A.; Chakraborty, D. Complimentary effects of annealing temperature on optimal tuning of functionalized carbon-V_2O_5 hybrid nanobelts for targeted dual applications in electrochromic and supercapacitor devices. *Rsc Adv.* **2018**, *8* (16), 8596−8606.

(49) Wu, L. L.; Camacho-Alanis, F.; Castaneda, H.; Zangari, G.; Swami, N. Electrochemical impedance spectroscopy of carboxylic-acid terminal alkanethiol self assembled monolayers on GaAs substrates. *Electrochim. Acta* **2010**, *55* (28), 8758−8765.

(50) Shimizu, M.; Ohnuki, T.; Ogasawara, T.; Banno, T.; Arai, S. Electrodeposited Cu/MWCNT composite-film: a potential current collector of silicon-based negative-electrodes for Li-Ion batteries. *Rsc Adv.* **2019**, *9* (38), 21939−21945.

(51) Guo, Q. F.; Li, J. J.; Zhang, B.; Nie, G. M.; Wang, D. B. High-Performance Asymmetric Electrochromic-Supercapacitor Device Based on Poly(indole-6-carboxylicacid)/TiO_2 Nanocomposites. *ACS Appl. Mater. Interfaces* **2019**, *11* (6), 6491−6501.

(52) Qiu, M. J.; Zhou, F. W.; Sun, P.; Chen, X. B.; Zhao, C. X.; Mai, W. J. Unveiling the electrochromic mechanism of Prussian Blue by electronic transition analysis. *Nano Energy* **2020**, *78*, 105148.

(53) Zhang, G. G.; Lu, K. K.; Zhang, X. C.; Yuan, W. J.; Shi, M. Y.; Ning, H. L.; Tao, R. Q.; Liu, X. Z.; Yao, R. H.; Peng, J. B. Effects of Annealing Temperature on Optical Band Gap of Sol-gel Tungsten Trioxide Films. *Micromachines* **2018**, *9* (8), 377.

(54) Zhang, Y. F.; Jing, X. Y.; Wang, Q. S.; Zheng, J. Q.; Jiang, H. M.; Meng, C. G. Three-dimensional porous V_2O_5 hierarchical spheres as a battery-type electrode for a hybrid supercapacitor with excellent charge storage performance. *Dalton Trans.* **2017**, *46* (43), 15048−15058.

(55) (55a) Yue, Y.; Li, H.; Li, K.; Wang, J.; Wang, H.; Zhang, Q.; Li, Y.; Chen, P. High-performance complementary electrochromic device based on $WO_3 \cdot 0.33H_2O$/PEDOT and prussian blue electrodes. *J. Phys. Chem. Solids* **2017**, *110*, 284−289. (55b) Jeong, C. Y.; Kubota, T.; Tajima, K.; Kitamura, M.; Imai, H. Complementary electrochromic devices based on acrylic substrates for smart window applications in aircrafts. *Mater. Chem. Phys.* **2022**, *277*, 125460.

(56) Bae, J.; Seo, D. G.; Park, S. M.; Park, K. T.; Kim, H.; Moon, H. C.; Kim, S. H. Optimized low-temperature fabrication of WO_3 films for electrochromic devices. *J. Phys. D: Appl. Phys.* **2017**, *50* (46), 465105.

(57) Bi, Z. J.; Li, X. M.; Chen, Y. B.; He, X. L.; Xu, X. K.; Gao, X. D. Large-Scale Multifunctional Electrochromic-Energy Storage Device Based on Tungsten Trioxide Monohydrate Nanosheets and Prussian White. *ACS Appl. Mater. Interfaces* **2017**, *9* (35), 29872−29880.

(58) Wang, W. Q.; Wang, X. L.; Xia, X. H.; Yao, Z. J.; Zhong, Y.; Tu, J. P. Enhanced electrochromic and energy storage performance in mesoporous WO_3 film and its application in a bi-functional smart window. *Nanoscale* **2018**, *10* (17), 8162−8169.

(59) Li, H. Z.; Firby, C. J.; Elezzabi, A. Y. Rechargeable Aqueous Hybrid Zn^{2+}/Al^{3+} Electrochromic Batteries. *Joule* **2019**, *3* (9), 2268−2278.

(60) Ding, Y. L.; Wang, M. Y.; Mei, Z. Y.; Diao, X. A. Novel Prussian White@MnO_2-Based Inorganic Electrochromic Energy Storage Devices with Integrated Flexibility, Multicolor, and Long Life. *ACS Appl. Mater. Interfaces* **2022**, *14* (43), 48833−48843.

(61) Zhang, S. L.; Peng, Y. T.; Zhao, J.; Fan, Z. J.; Ding, B.; Lee, J. Y.; Zhang, X. G.; Xuan, Y. M. Amorphous and Porous Tungsten Oxide Films for Fast-Switching Dual-Band Electrochromic Smart Windows. *Adv. Opt. Mater.* **2023**, *11* (1), 8.

(62) Wang, B.; Cui, M. W.; Gao, Y. F.; Jiang, F. Y.; Du, W.; Gao, F.; Kang, L. T.; Zhi, C. Y.; Luo, H. J. A Long-Life Battery-Type Electrochromic Window with Remarkable Energy Storage Ability. *Sol. RRL* **2020**, *4* (3), 9.

(63) Song, J. S.; Huang, B. K.; Xu, Y. Y. J.; Yang, K. J.; Li, Y. F.; Mu, Y. Q.; Du, L. Y.; Yun, S.; Kang, L. T. A Low Driving-Voltage Hybrid-Electrolyte Electrochromic Window with Only Ferreous Redox Couples. *Nanomaterials* **2023**, *13* (1), 213.

(64) Sun, B. L.; Liu, Z. X.; Li, W.; Huang, H.; Xia, Y.; Gan, Y. P.; Liang, C.; Zhang, W. K.; Zhang, J. A high-performance electrochromic battery based on complementary Prussian white/$Li_4Ti_5O_{12}$ thin film electrodes. *Sol. Energy Mater. Sol. Cells* **2021**, *231*, 111314.

(65) Chen, P. W.; Chang, C. T.; Ko, T. F.; Hsu, S. C.; Li, K. D.; Wu, J. Y. Fast response of complementary electrochromic device based on WO_3/NiO electrodes. *Sci. Rep.* **2020**, *10* (1), 8430.

(66) Pan, J. B.; Zheng, R. Z.; Wang, Y.; Ye, X. K.; Wan, Z. Q.; Jia, C. Y.; Weng, X. L.; Xie, J. L.; Deng, L. J. A high-performance electrochromic device assembled with hexagonal WO_3 and NiO/PB composite nanosheet electrodes towards energy storage smart window. *Sol. Energy Mater. Sol. Cells* **2020**, *207*, 110337.

(67) Xu, B.; Chen, J.; Li, P.; Ouyang, Y.; Ma, Y.; Wang, H.; Li, H. Transparent metal oxide interlayer enabling durable and fast-switching zinc anode-based electrochromic devices. *Nanoscale* **2023**, *15* (48), 19629−19637.

(68) Hu, J.; Zhang, Y.; Xu, B.; Ouyang, Y.; Ma, Y.; Wang, H.; Chen, J.; Li, H. A hydrophobic alloy-coated Zn anode for durable electrochromic devices. *Chem. Commun.* **2024**, *60*, 566−569.

(69) Li, H.; Elezzabi, A. Y. Simultaneously enabling dynamic transparency control and electrical energy storage via electrochromism. *Nanoscale Horiz.* **2020**, *5* (4), 691−695.

(70) Li, H.; Zhang, W.; Elezzabi, A. Y. Transparent Zinc-Mesh Electrodes for Solar-Charging Electrochromic Windows. *Adv. Mater.* **2020**, *32* (43), 2003574.

■ NOTE ADDED AFTER ASAP PUBLICATION

Due to a production error, this paper was published ASAP on March 25, 2024, with an error in formula 1. The corrected version was reposted on March 28, 2024.